ChemCatChem

Review
doi.org/10.1002/cctc.202400100

Chemistry Europe
European Chemical Societies Publishing

www.chemcatchem.org

Reaction Mechanisms of Single Metal Site Catalysts Supported on Covalent Organic Frameworks

Aswin Gopakumar,[a] Manuel A. Ortuño,*[b] and Julio Lloret-Fillol*[a, c]

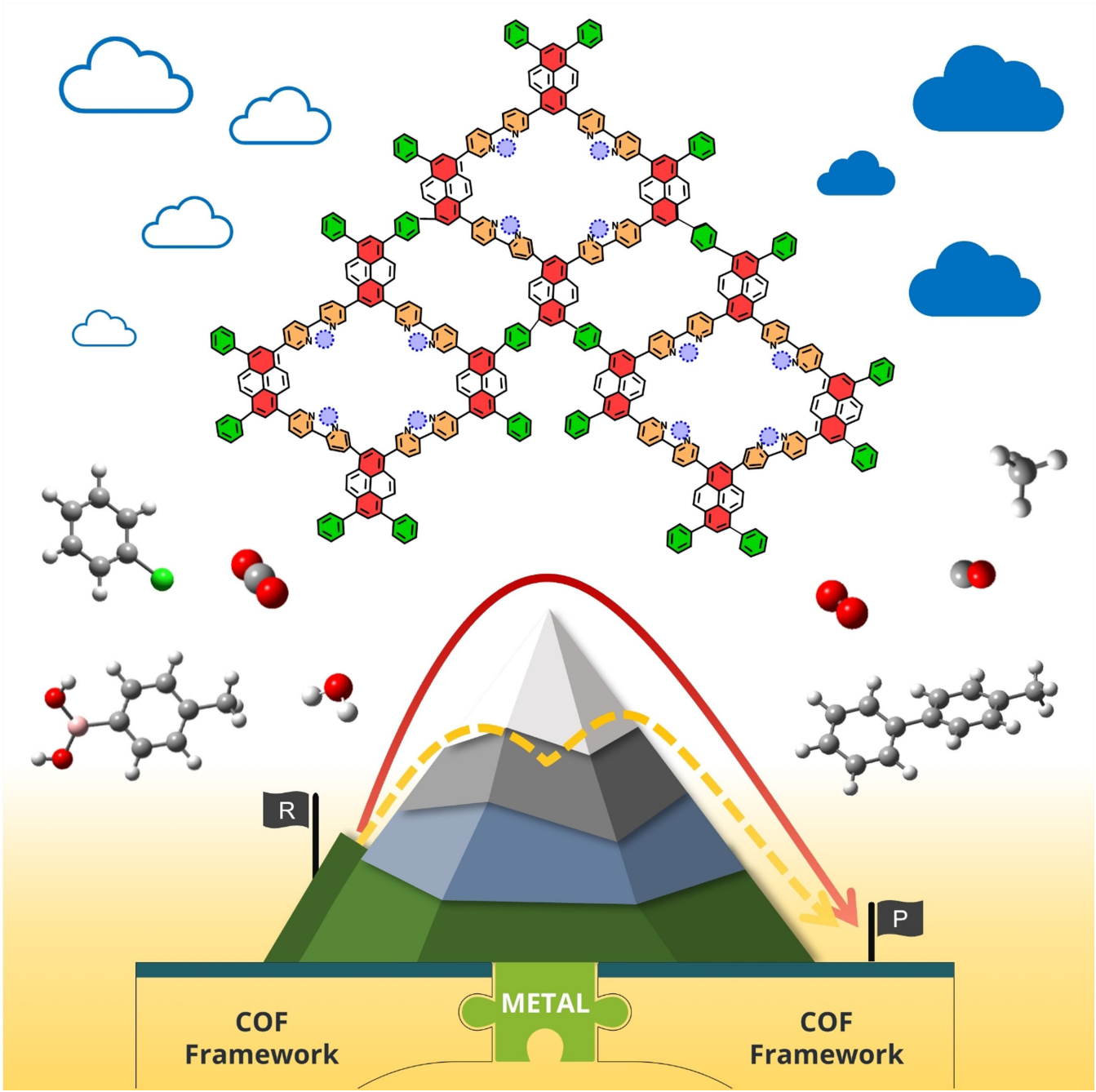

Covalent organic frameworks (COFs) have become a versatile platform to immobilize a wide variety of single-atom metal catalysts. The resulting post-synthetic modified materials present a spectrum of valuable properties ranging from homogeneous to heterogeneous systems, such as well-defined catalytic sites, selectivity, recyclability, and stability. In this minireview, we discuss selected contributions that provide experimental and computational details on reaction mechanisms (e.g., via EXAFS, TEM, and DFT) catalyzed by single-atom metals embedded within the COF structure. When applicable, we highlight the different behaviour between molecular (homogeneous) and COF-supported (heterogeneous) sites regarding catalytic performance. With this survey, we aim to decipher the key features that aid in seeing COFs as not merely passive supports but as active items in catalysis.

1. Introduction

Reticular chemistry relies on the controlled assembly of synthetic subunits to design well-defined porous materials.[1] This approach allows for fine-tuning material properties, such as chemical composition, surface area, and pore size. Among the different families of porous materials, here we focus on covalent organic frameworks (COFs).[1] COFs are a class of crystalline, lightweight, and porous materials constructed through strong covalent bonding of organic building blocks (subunits). These frameworks are notable for their highly ordered structures, which can be two-dimensional or three-dimensional, tailored through the reticular synthesis of carefully chosen building blocks.[2,3] This unique molecular architecture facilitates precise spatial arrangement and robustness, making COFs ideal for a variety of applications such as gas storage, separation processes, and catalysis. Moreover, the large access to potential organic building blocks allows for fine-tuning of physical and chemical properties to meet specific needs, making them very versatile materials. These properties contributed to its rapid development in the last decade dramatically impacting all fields of chemistry,[4,5] and particularly, heterogeneous catalysis.[6,7]

Covalent organic frameworks can be catalysts themselves[8] or act as catalyst supports,[9,10] hosting nanoparticles or anchoring molecular species. The precise control exerted into the framework allows for designing chemical environments suitable for post-synthetic modification and functionalization.[11] As such, these materials have become a great asset in preparing single-site metal catalysts.[12] These syntheses typically involve two pathways – (i) post-synthetic solvothermal metalation of the COF utilizing different metal precursors, or (ii) using, in the synthesis of the COF, metal complexes directly as COF subunits (Figure 1). When excluding building subunits that already contain metal atoms, such as porphyrins and phthalocyanines, the metalation usually occurs at the edges of the framework where functional groups are available, rather than the corners where aromatic units reside (Figure 1). Both pathways have advantages and problems, the former can lead to uncoordinated metal precursors while the latter can only be employed when metal complexes are stable under the usually demanding COF synthetic routes. However, regardless of the synthetic process, it is desirable to have a high reproducibility on the metal incorporation within the COF, including reproducibility on catalytic site density and distribution. Furthermore, the strategy should anticipate control over the metal complex coordination sphere resulting during the synthesis. Regarding the coordination and relative position of the well-defined metal centers within the framework, they can be classified as either corners or edges. Corners refer to the core structural units within the COF, typically consisting of multifunctional organic molecules acting as vertices where building blocks converge, thus defining the geometry of the framework. Edges, on the other hand, comprise the molecules that connect these corners, influencing the porosity and topology of the COF. This distinction underscores the local chemical environment as a pivotal factor in controlling the exposition of active catalyst sites. Therefore, here we will focus the attention on reported COFs where the metal sites are well-exposed.

Moreover, such immobilization of molecular-like species into a solid framework merges the high selectivity and tunability of homogeneous catalysts with the stability and recyclability of heterogeneous systems (Figure 2). More interestingly, the COF does not frequently play an innocent role, thus

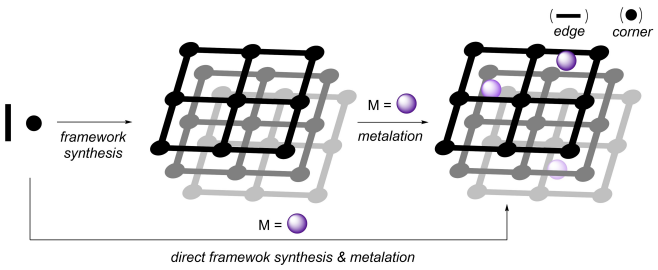

Figure 1. Schematic post-synthetic and direct metalation of COFs.

[a] *Dr. A. Gopakumar, Prof. J. Lloret-Fillol*
Institute of Chemical Research of Catalonia (ICIQ), The Barcelona Institute of Science and Technology (BIST)
Avinguda Països Catalans 16, 43007, Tarragona, Spain
E-mail: jlloret@iciq.es

[b] *Dr. M. A. Ortuño*
Centro Singular de Investigación en Química Biolóxica e Materiais Moleculares (CIQUS), Universidade de Santiago de Compostela
Jenaro de la Fuente s/n, 15782 Santiago de Compostela, Spain
E-mail: manuelangel.ortuno@usc.es

[c] *Prof. J. Lloret-Fillol*
Institution for Research and Advanced Studies (ICREA)
Passeig Lluís Companys 23, 08010, Barcelona, (Spain)

Supporting information for this article is available on the WWW under https://doi.org/10.1002/cctc.202400100

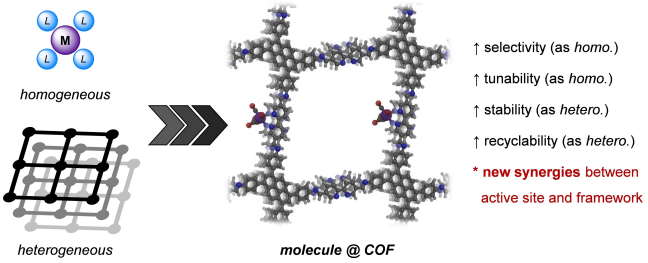

Figure 2. Heterogenization of molecular species in solid frameworks.

new synergies between the metal active site and the support can be exploited to enhance catalysis.

Indeed, the growth of COFs as platforms for single-atom metal catalysts is clearly demonstrated by their coverage in recent years. For instance, Guan et al.[13] reported a comprehensive review of the synthesis and applications of metalated COFs; Salemi et al.[14] collected Pd catalysts immobilized into COFs; Daliran et al.[15] gathered porous materials as catalysts for C–H bond activation and functionalization; and Wang et al.[16] as well as López-Magano et al.[17] surveyed COF materials for photocatalytic applications.

However, less attention has been devoted to the thorough examination of reaction mechanisms within these materials. It is typically assumed that the same or equivalent mechanism applies to molecular (homogeneous) and COF-supported (heterogeneous) catalysts, but that is not necessarily the case. For instance, from the phenomenological point of view, there are examples of frameworks that significantly modify the catalytic activity of the metal site, control the product selectivity, or shut down deactivation pathways.[18,19] Further understanding of these fascinating alterations of catalytic behaviour is essential to further exploit them. To this end, efforts are delving deeper into the mechanistic features of COFs, and a combination of both reaction experimental and computational techniques is often necessary (chemical reactivity, kinetics, IR, UV-Vis, EXAFS, TEM, and DFT, among others).

In this minireview, we have selected recent contributions of single metal site catalysts anchored to COFs, focusing on those where the metal sites are at the edges of connecting subunits (Figure 1), which provide detailed insights into the role of the framework in the reaction mechanism. We have also considered COFs based on triazine units (CTFs) despite some of them presenting low crystallinity, and we have excluded COFs based on macrocyclic MN_4 metal sites, such as porphyrins and phthalocyanines, which usually are at the corners of the frames and have been covered somewhere else.[20–24] We present the main conclusions and discuss the role of the framework in the catalytic process.

2. Mechanistic Studies on Single Metal Sites in COFs

Here, we collect selected contributions where detailed mechanistic information has been obtained through experimental and/or computational techniques. We divide them according to the type of reaction under study: (i) photo/electro CO_2 reduction, (ii) oxygen evolution and reduction, and (iii) organic transformations.

2.1. CO_2 Reduction

CO_2 photo- and electroreduction is a topic of great interest nowadays. The fact that there are plenty of value-added CO_2 reduction products implies a significant number of potential suitable catalysts and their fundamental understanding is of paramount interest. Single metal site COFs are seen as one of the latest generations of materials that can facilitate CO_2

Prof. Julio Lloret-Fillol is currently an ICREA professor and group leader at ICIQ (Spain) since 2014, where he is involved in homogeneous and heterogeneous photo- and electrocatalysis research. He obtained his PhD from the University of Valencia (Spain) in 2006 and then moved to the University of Heidelberg (Germany) as a MEyC and later as a Marie Curie postdoctoral fellow before joining as a Ramon y Cajal group leader at the University of Girona and then at ICIQ.

Dr Aswin Gopakumar is a Marie Curie postdoctoral fellow at ICIQ (Spain) since 2023, where he is involved in heterogeneous photo and electrocatalysis research. He obtained his PhD from EPFL (Switzerland) in heterogeneous catalytic CO_2 reduction research in 2018. Afterwards, he moved to the University of Antwerp (Belgium) as an IOF postdoctoral fellow until mid-2022. In late 2022, he joined ICIQ for another postdoctoral stay.

Dr Manuel A. Ortuño is currently a Distinguished Researcher at CIQUS in Universidad de Santiago de Compostela (Spain) since 2020, where he is involved in the simulation of homogeneous and porous chemical systems for catalysis. He obtained his PhD from the Universitat Autònoma de Barcelona (Spain) in 2014, and then moved to the University of Minnesota (USA) in 2015 and ICIQ (Spain) in 2018 for postdoctoral stays.

reduction through electrochemical and photochemical methods. Figure 3 shows various single-site metal-loaded COFs (M–COFs) used in CO_2 reduction reactions (CO_2RRs).

Lu et al. reported a series of metal-loaded (Co, Ni, and Zn) based on DQTP (2,6-diaminoanthraquinone-2,4,6-triformylphloroglucinol, Figure 3a) for the photocatalytic CO_2RR to produce HCOOH or CO using $[Ru(bpy)_3]Cl_2$ (bpy = bipyridine) as photosensitizer and triethanolamine as an electron donor.[25] The Co variant exhibits a high selectivity towards CO production with a rate of 1020 μmol h^{-1} g^{-1} whereas the Zn variant was found to selectively produce HCOOH with a production rate of 153 μmol h^{-1} g^{-1}. The Ni variant produces intermediate selectivity and yields. The study further investigates the integration of earth-abundant metals into COFs for photocatalytic CO_2RR. Using density functional theory (DFT), it focuses on the interaction between Zn and the DQTP–COF structure. It reveals that Zn binds with quinone oxygen atoms in the COF, leading to stronger bonding and altered interlayer distances, indicative of coordination bonding. This mechanism is crucial for enhancing the semiconductor properties of the COFs, thereby improving their efficiency in photocatalytic CO_2RR. Transition metals such as Co(II), Ni(II), and Zn(II) were successfully embedded into the frameworks, significantly affecting physical properties such as pore size and surface area, with metal content quantified around 6–7 wt%. The integration of metals was experimentally confirmed through X-ray photoelectron spectroscopy (XPS) and supported by DFT calculations, which identified potential binding sites and indicated strong interlayer interactions. Stability assessments included thermogravimetric analysis (TGA) and microscopic analyses (SEM and TEM), which demonstrated robustness and preservation of the COF structure post metal-loading. Furthermore, photocatalytic performance tests indicated that these materials, particularly DQTP COF–Co, maintained high catalytic activity and structural integrity even after several recycling processes, underscoring their durability and functional stability.

Likewise, Zhong et al. proposed single Ni sites within the COF derived from triformylbenzene and diaminobipyridine (Figure 3b) that could achieve a CO production rate of 4057 μmol g^{-1} in a 5 h reaction with a 96% selectivity over H_2 evolution under photocatalytic conditions.[26] For the photocatalytic studies, $[Ru(bpy)_3]Cl_2$ was the photosensitizer and triethanolamine was the electron donor employed. In addition, bpy was also added to the reaction. The authors proposed based on DFT calculations that (N_4)Ni (N_2 from the COF and N_2 from the bpy) was the active site, but no direct spectroscopic evidence was reported. Ni-TpBpy was synthesized by treating TpBpy with $Ni(ClO_4)_2 \cdot 6H_2O$ in acetonitrile, resulting in a Ni content of 0.3 mmol g^{-1}. Ni ions were confirmed via $Ni(ClO_4)_2$ treatment, evidenced by XPS and energy-dispersive X-ray spectroscopy (EDX) mapping which showed Ni^{2+} peaks and homogeneous Ni distribution. Metal binding sites are experimentally validated using HAADF-STEM, displaying bright spots indicative of atomically dispersed Ni centers. The framework's stability is demonstrated through repeated photocatalytic cycles, maintaining structural integrity and chemical consistency, as shown by minimal changes in Fourier transform infrared (FTIR) and XPS spectra after use, confirming both the robustness and efficiency of Ni-TpBpy in catalytic applications.

Das et al. reported a novel Co(II)-loaded COF based on triformylphluroglucinol and trihydrazinotriazine (Figure 3c) that can fix CO_2 to amines to generate *N*-formylated products under visible light with a TON of 114.[27] This catalyst system offers excellent catalytic activity, selectivity, and recyclability at least up to 5 times for the sustainable one-pot synthesis of *N*-formylated products from CO_2. The Co(II)@Tp-TH COF photocatalyst features a cobalt(II) loading of 4.9 wt% as determined by atomic absorption spectroscopy (AAS). Metal binding sites within this material were confirmed using X-ray photoelectron spectroscopy, which showed specific binding energies indicative of cobalt interacting with nitrogen atoms in the framework, and FTIR, where shifts in N–H stretch bands suggested interactions between cobalt ions and nitrogen groups. The stability of the catalyst was evidenced by its thermal robustness up to 370 °C, as shown by TGA, and its ability to maintain structural integrity and performance after multiple uses, confirming its suitability for practical applications in catalysis.

Cheng et al. reported another Re-loaded COF (Re–COF) based on trimethyltriazine and bis(formyl)bipyridine (Figure 3d) that can give photocatalytic CO production rate (190.6 μmol g^{-1} h^{-1} with about 100% selectivity) and O_2 evolution (90.2 μmol g^{-1} h^{-1}) among all the porous catalysts in CO_2 reduction with H_2O as sacrificial agents.[28] DFT calculations show the catalytic action of Re-complex in COFs, creating a ligand-to-metal charge-transfer channel. Photon absorption triggers charge transfer from the triazine ring to Re-bpy in Re–COF, efficiently separating HOMO and LUMO. This separation aids CO_2 reduction via excited electrons moving to Re-bpy, and H_2O oxidation through holes in the triazine ring. For CO_2 reduction in Re–COF, CO_2 is activated by Re, forming *COOH through a proton-coupled electron transfer. The formation of *COOH, the key step, has a 0.71 eV energy barrier. *COOH then transforms into *CO, releasing CO. In H_2O oxidation, the process starts with H_2O dissociating into *OH, facilitated by N in the triazine ring. *OH turns into *O, which combines with H_2O to form *OOH, the crucial step with a 1.73 eV barrier. O_2 is finally produced after proton removal from *OOH. The M–COF features a metal loading of 13.5% by weight, quantified using ICP-OES. Experimental confirmation of metal binding sites within the COF was achieved using FTIR spectroscopy, solid-state ^{13}C NMR, and XPS, which verified the structural integration and chemical state of the rhenium complexes. The material demonstrated excellent stability and durability, maintaining high catalytic efficiency over 50 h of operation and retaining about 90% of its initial activity after multiple cycles, showcasing its robustness in photocatalytic applications for CO_2 reduction.

Zhang et al. reported a Cu(II)-loaded COF based on tris(aminophenyl) triazine and bipyridine dicarboxaldehyde (Figure 3e, Cu-Bpy–COF) that can demonstrate significant improvements in photocatalytic CO_2 reduction.[29] The Cu-Bpy–COF enhanced CH_4 yield to 70.0 μmol g^{-1} and CO yield to 6.4 μmol g^{-1}, compared to 45.9 μmol g^{-1} and 13.0 μmol g^{-1}, respectively, for pristine Bpy–COF. The best CH_4 evolution rate was achieved with 10 mg of Cu-Bpy–COF. When using DMF as a

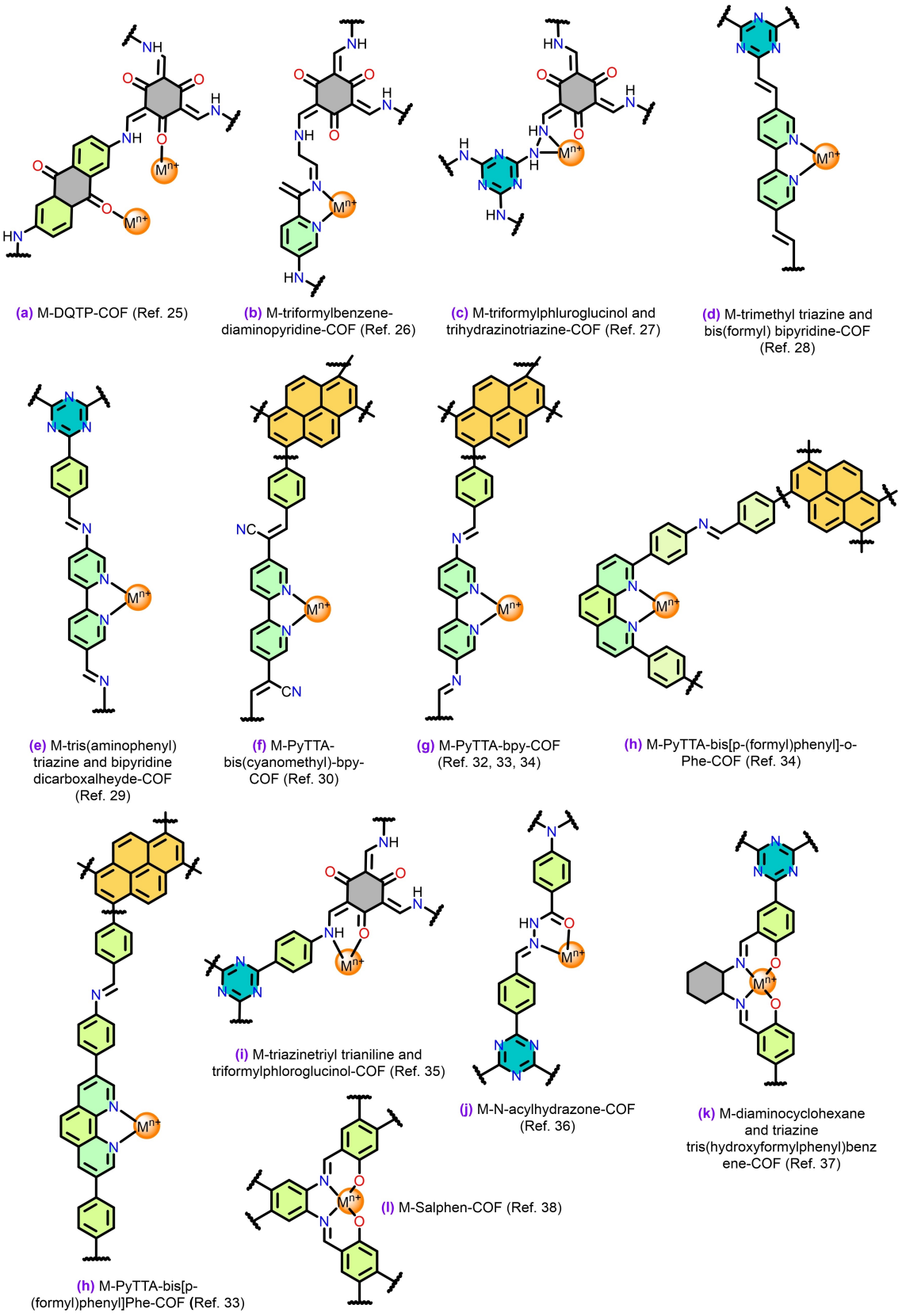

Figure 3. Single-site metal-loaded COFs used in CO_2RRs. n = 0, 1, 2, etc.

solvent, CO production reached 40.8 μmol g^{-1} with nearly 100% selectivity, and up to 90.0 μmol g^{-1} with 66.4% selectivity at a 50% DMF ratio. Cu-Bpy–COF showed a higher CO_2 uptake of 14.7 $cm^3 g^{-1}$ than Bpy–COF (9.2 $cm^3 g^{-1}$). DFT calculations revealed that the LUMO of Cu-Bpy–COF mainly localized on Cu-Bpy moieties, facilitating charge separation and enhancing photocatalytic performance. This study highlights the pivotal role of single Cu sites in CO_2 adsorption and reduction, offering nearly 100% selectivity for CO or CH_4 by modifying the reaction media. Triethylamine, serving as both hole sacrificial agent and proton transfer catalyst, further boosts the CO_2 reduction efficiency, underscoring the potential of COF-based photocatalysts with non-noble metal single sites for selective CO_2 reduction. The Cu-Bpy–COF material incorporates single Cu sites with a metal loading of about 8.3 wt%, confirmed using techniques such as FT-IR, solid-state NMR, XPS, diffuse reflectance infrared Fourier transform spectroscopy (DRIFTS), and XAS, which validated the coordination of Cu to nitrogen sites and detailed the electronic and atomic environment. Stability assessments through TGA showed the framework's thermal stability up to 500 °C, and PXRD confirmed the maintenance of its crystalline structure post-metal incorporation. Photostability tests indicated minimal Cu leaching, with the structure and catalytic performance of the COF remaining robust across multiple cycles of CO_2 reduction, demonstrating good operational stability.

A Re-loaded COF based on tetrakis(4-formylphenyl)pyrene and bis(cyanomethyl) bipyridine ligands (Figure 3f) was investigated by Fu et al. that can achieve a maximum rate of 1040 mmol $g^{-1} h^{-1}$ for CO production with 81% selectivity.[30] CO production rates were further increased up to 1400 mmol $g^{-1} h^{-1}$, with an improved selectivity of 86% when a photosensitizer was added. Photophysics of the system was studied by transient absorption spectroscopy (TAS). The COF was chemically modified by loading with 18 wt% of the rhenium complex [$Re(CO)_5Cl$], which ligated half of the available bipyridine sites within the framework. This metal integration was experimentally verified using PXRD and STEM combined with EDX, which confirmed the uniform distribution and structural incorporation of Re. Further evidence was provided by FTIR spectroscopy, indicating characteristic CO-stretching bands of the Re complex. The material demonstrated good stability under photocatalytic conditions, retaining crystallinity and functionality over extended periods of visible light illumination, although a decline in crystallinity and activity was noted after 50 h, pointing to challenges in long-term stability. In solution, excitation upon irradiation forms a metal-to-bipyridine excited state (^{3}MLCT) which is then quenched by an electron donor.[31] However, the COF differs from the homogenous catalysts. The authors proposed a pyrene excitation to a bipyridine-based LUMO. The presence of the Re center within the COF leads to the formation of a long-lived charge-separated (non-emissive) state.

Bandomo et al. reported a single-site Mn–COF based on (pyrenetetrayl)tetraaniline and bipyridyl dialdehyde (Figure 3g) that shows a low CO_2RR onset potential of 190 mV and high current densities (> 12 mA·cm^{-2}, at 550 mV overpotential) in water (Figure 4).[32] TOF_{CO} and TON_{CO} values are as high as 1100 h^{-1} and 5800 (after 16 h), respectively, which are more than 10-fold higher than those obtained for the equivalent Mn-based molecular catalyst reported until then. IR and extended X-ray absorption fine structure (EXAFS) spectra were used to identify the coordination of the Mn resulting equivalent within the COF to the homogeneous complex in solution {*fac*-Mn-$(N_2)(CO)_3S$; S = solvent}. Catalytic intermediates were characterized and *in situ* monitoring of electrochemically active COF by ATR-IR spectroelectrochemistry. Although ATR-IR-SEC can serve to elucidate metal CO_2RR intermediates, this was the first time employed in the study of a COF, and it is still rarely employed. In addition, DFT calculations were also essential to identify the key intermediates. Noteworthy, the authors proposed that the COF imposes mechanical constraints on the {*fac*-$Mn(CO)_3S$} centers, offering a strategy to avoid forming the detrimental dimeric $Mn^0 - Mn^0$, which is a resting state typically observed for the homologous molecular complex. The absence of dimeric species correlates with catalytic enhancement. The COFbpyMn demonstrates a high Mn loading of approximately 85%, confirmed using ICP-OES. The metal binding sites within the COF were meticulously characterized through FTIR, XPS, and XAS, ensuring accurate metal incorporation and coordination. Additionally, the stability of the material was validated through TGA and PXRD, which established its robustness and consistent catalytic activity, further evidenced by stable performance in extended cyclic voltammetry (CV) tests. These attributes underscore the material's effectiveness for electrocatalytic applications. Recently, the same group reported another Mn-based COF specifically COFbpyMn (with bipyridine linker, as in the previously mentioned one) and COFPTMn (with phenanthroline linker), tailored for electrocatalytic CO_2 reduction.[33] COFbpyMn stands out with superior electrochemical CO_2 reduction activity due to its high crystallinity and porosity, significantly enhancing catalytic efficiency over its molecular analogs non-covalently immobilized on carbon electrodes. COFPTMn, which employs a larger phenanthroline linker, demonstrates heightened catalytic activity at near-neutral pH but is hindered by reduced crystallinity and porosity, impacting overall performance. The electrochemical testing reveals that COFPTMn achieves a CO_2 reduction onset potential of −1.0 V vs SCE and produces CO as the predominant product with a Faradaic efficiency of 30% for CO and 15% for formate. These frameworks stabilize Mn(I) radical anion intermediates, effectively preventing $Mn^0 - Mn^0$ dimer formation through the electronic and steric features of the COF structure. This setup promotes a highly efficient CO_2 reduction mechanism influenced by the COFs' structural properties, resulting in enhanced catalytic activity. The metal loading was quantitatively determined using ICP-OES, revealing that 38 mg of Mn per gram of COF was incorporated, accounting for the metalation of approximately 36% of the available phenanthroline sites. The metal binding sites were experimentally confirmed via ATR-FTIR spectroscopy, which displayed characteristic CO stretching frequencies at 2027 and 1922 cm^{-1}, indicative of {$Mn(CO)_3Br$} moieties in a facial coordination geometry within the COF backbone. Stability assessments through TGA showed two major decomposition steps, with the

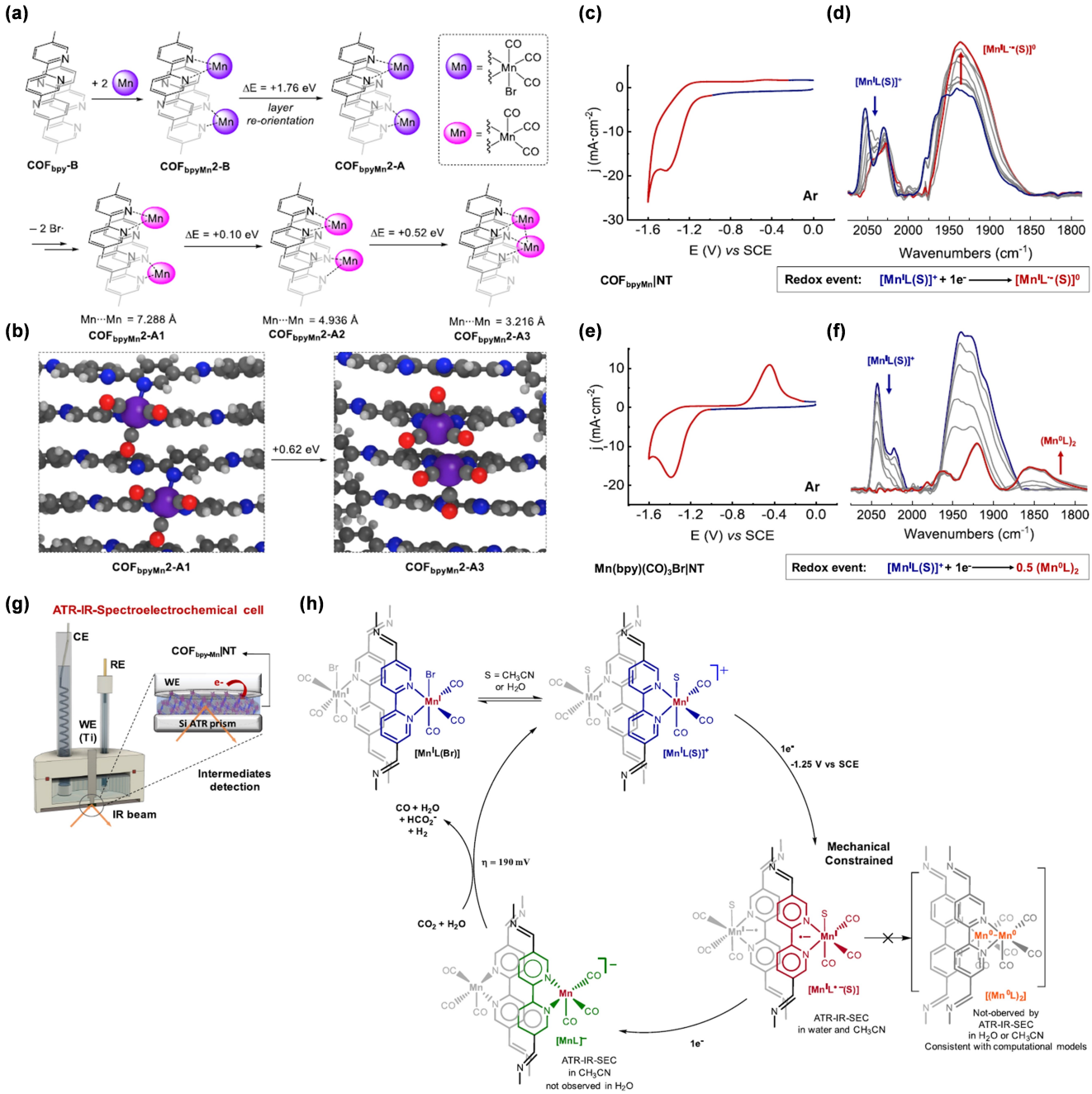

Figure 4. DFT energies for the (a) endergonic dimerization mechanism process within the COF material and (b) optimized structures for COF$_{bpyMn}$2-A1 and COF$_{bpyMn}$2-A3; comparison of CVs at 100 mV·s^{-1}(c, e) and ATR-IR absorbance potential dependent spectra of COFbpyMn | NT (d) and the model 1 | NT (f) in water (0.5 M NaHCO$_3$) under Ar at room temperature; (g) schematic representation of the ATR-IR-SEC cell and (h) the proposed catalytic cycle for COFbpyMn in the based on computational models and spectroelectrochemical data. Reprinted with permission from Ref. [32] Copyright 2021, American Chemical Society.

initial step likely due to the release of CO ligands from Mn centers, and PXRD patterns confirmed the crystalline integrity post-metalation, though with reduced crystallinity compared to other analogs. These elements highlight the COF's structural design tailored for enhanced CO_2 reduction performance.

Zou et al. presented a study on enhancing CO_2 photoreduction using one-dimensional COFs synthesized by the Schiff base condensation of pyrene tetrayltetraaniline (PyTTA) and 2,2'bipyridine-5,5'-dicarbaldehyde (2D COFs, Figure 3g) and bis[p-(formyl)phenyl] phenanthroline (1D COFs, Figure 3h) supporting Co(II) sites.[34] They found that 1D–COFs, especially PyTTA–COF, have superior CO_2 photoreduction capabilities compared to 2D versions. This enhancement is linked to the edge microstructures in 1D–COFs, which stabilize the structure, minimize energy loss during exciton dissociation, and facilitate effective charge transfer. Specifically, the 1D-PyTTA–COF, when combined with Co ions, achieved an impressive CO evolution rate of 1003 μmol g^{-1} in 8 h under visible light. This research not only offers a solution to charge transfer issues in COFs but also underscores the importance of controlling dimensionality

to boost photocatalytic efficiency. Additionally, DFT was employed to compare the electronic properties of 1D-PyTTA–COF to its 2D counterpart. These calculations show a distinct distribution in the HOMO and LUMO of the 1D-PyTTA–COF, contributing to its enhanced photocatalytic activity. Calculations of binding energy and systemic energy, based on the dihedral angle between interlayer benzene rings, provide further understanding of the stability and interactions within the COF structure. These theoretical findings corroborate the experimental results, emphasizing the pivotal role of edge microstructures in advancing CO_2 photoreduction. The presence of cobalt was validated through XPS and EXAFS, confirming the Co–N/O coordination within the frameworks. Stability assessments revealed that 1D PyTTA–COF displayed superior chemical and thermal stability, maintaining structural integrity and photocatalytic activity even after exposure to harsh chemical environments and repeated usage cycles. This robustness, combined with effective metal incorporation, highlights the potential of these COFs, particularly the 1D PyTTA–COF, in photocatalytic applications for CO_2 reduction.

Qiu et al. designed imine-linked COFs based on triazinetriyl trianiline and triformylphloroglucinol (Figure 3i) as the electron bridge that links the photocatalyst and the robust metal Co(II) active sites for photocatalytic CO_2RR.[35] When integrated with defective g-C_3N_4, the composite generated 37.3 mmol·h^{-1} of CO with 98.8% selectivity over H_2 evolution under visible light irradiation, which greatly outperformed other non-noble metal species as co-catalysts. The coupling of Co with COF ligands was analyzed with DFT, revealing that N–Co–O (0.54 eV) has a lower formation energy compared to N–Co–N (1.43 eV) and O–Co–O (0.83 eV). This supports the experimental findings where C=C–N and C=O groups in the bare COF preferentially form stable six-membered chelating rings with Co(II). The metal binding sites are confirmed through XPS, TEM, HAADF-STEM, and supported by DFT simulations, indicating preferential binding of Co to specific nitrogen and oxygen sites. The stability of these materials is demonstrated through consistent performance over multiple cycles of CO_2 photoreduction, highlighting their potential for practical photocatalytic applications.

Yang et al. reported a Ni-modified COF composed of *N*-acylhydrazone-linked electron-donor and electron-acceptor dyads (H–COF–Ni, Figure 3j) that can generate 5694 μmol g^{-1} of CO with 96% selectivity over H_2 evolution in 2 h under visible light irradiation, which greatly outperforms that of the typical imine-linked counterpart (I–COF–Ni).[36] DFT calculations were conducted through the carboxyl intermediates step. The CO_2 molecule presents the bent configuration after interacting with Ni centers, showing that the activation of CO_2 molecules could be realized on Ni active sites. Notably, the Ni–C bond length (3.074 Å) for H–COF–Ni is shorter than that of I–COF–Ni (3.277 Å), indicative of stronger binding interaction between CO_2 molecules and Ni active sites in H–COF–Ni. The adsorption energy of CO_2 on Ni is −0.58 eV for H–COF–Ni, which is more negative than that of I–COF–Ni (−0.28 eV). Such a large difference in the adsorption behaviour of CO_2 over Ni sites is mainly attributed to local microenvironments enabled by the linkages of H–COF and I–COF. It is generally accepted that stronger CO_2 adsorption is favourable for the activation of CO_2 and the stabilization of metal-CO_2 adducts. H–COF–Ni was characterized for its metal content, metal binding sites, and stability using various techniques. Metal loading was determined to be 0.050 mmol g^{-1} using ICP-AES. The metal binding sites were confirmed through XRD and FTIR, which indicated the incorporation and coordination of nickel ions within the framework. XPS further supported these findings by showing changes in binding energies. Stability assessments demonstrated that the material maintained its catalytic activity and selectivity over several cycles, with no significant changes observed in the FTIR spectrum, XRD pattern, or the high-resolution Ni 2p XPS spectrum, indicating the material's good durability under the tested conditions.

Yang et al. reported a Zn-Salen-based COF (Zn–S–COF) made from diaminocyclohexane and triazine tris(hydroxyformylphenyl)benzene (Figure 3k) that can drive a CO_2-to-CO conversion rate of 105.88 μmol g^{-1} h^{-1} under diluted CO_2 (15%) atmosphere.[37] Moreover, the natural sunlight-driven diluted CO_2 reduction rate also reaches 126.51 μmol g^{-1} in 5 h. Further experiments and theoretical calculations reveal that the triazine ring in the Zn–S–COF promotes the activity of H_2O oxidation and CO_2 reduction sites, and the loaded ILs provide an enriched CO_2 atmosphere, realizing the efficient photocatalytic activity in diluted CO_2 reduction. The Zn–S–COF contains approximately 7.20 wt% zinc, determined through ICP-OES. Experimental confirmation of the zinc-binding sites was achieved using XAS, including X-ray absorption near-edge structure (XANES) and EXAFS analyses. These studies revealed that zinc is stably coordinated by two nitrogen and two oxygen atoms, forming a Zn-N_2O_2 coordination configuration. Stability assessments via TGA showed that Zn–S–COF is thermally stable up to 280 °C and maintains chemical integrity after immersion in various solvents and across a range of pH conditions for 7 days, as evidenced by consistent PXRD patterns post-testing.

Zhu et al. introduced a π-conjugated van der Waals heterostructure, which combines polymeric carbon nitride (p-CN) with a Ni(II)-containing Salphen-based COF based on trithiocyanuric acid, hydroxyterephthalaldehyde, benzenetetraamine tetrahydrochloride (Ni–COF, Figure 3l), revealing enhanced photocatalytic activity.[38] The heterostructure exhibited a faster exciton annihilation decay lifetime compared to neat polymeric carbon nitride (p-CN), indicating efficient electron transfer. Photocatalytic tests showed a hydrogen generation rate of 2.3 mmol g^{-1} h^{-1} and CO generation of 6.2 μmol g^{-1}·h^{-1}, outperforming neat p-CN by approximately 127 times for H_2 and 3 times for CO. This indicates a promising approach for solar fuel production using such heterostructures. DFT calculations reveal a work function of 4.69 eV for p-CN and 4.36 eV for Ni–COF. This difference in work functions drives electrons from Ni–COF to p-CN, creating a built-in electric field that enhances charge separation efficiency. DFT also indicates that single Ni sites in Ni–COF are effective for proton reduction, vital for the heterostructure's improved photocatalytic performance. The metal loading was executed with Ni at a weight percentage of 3%, optimizing the photocatalytic efficiency of the material. The metal binding sites, specifically the single-atom Ni sites,

were confirmed experimentally through XAS and EXAFS analyses, which revealed Ni–N and Ni–O bonding configurations. Stability assessments demonstrated that the p-CN/Ni–COF heterostructure maintained structural integrity and catalytic performance over repeated photocatalytic cycles, supported by unchanged XRD and FTIR post-testing. These factors illustrate a well-synthesized material capable of efficient charge separation and enhanced photocatalytic activity under visible light.

Ai et al. introduced Co(II)-infused covalent organic framework (Co–COF), synthesized with biphenyl tetracarbaldehyde and (benzothiadiazolediyl)bis[benzenamine] ligands. This Co–COF effectively converts CO_2 to CO, achieving a high rate of 2423 $\mu mol\,g^{-1}\cdot h^{-1}$ and over 99% selectivity under visible light.[39] The CO_2 reduction involves stages of $*CO_2$ and *COOH formation, followed by CO release (with * denoting the adsorption site). Energy requirements for $*CO_2$ formation are 0.21 eV for the bare COF and 0.42 eV for Co–COF. The transition from $*CO_2$ to *COOH in Co–COF is more energy-efficient (0.21 eV) compared to the bare CO (1.31 eV). This indicates that Co–COF, with the added CoO, enhances charge migration and CO_2 reduction efficiency. Both Co–COF and bare COF require similar energy for the *COOH to *CO transition, but the bare COF is more efficient in converting *CO to CO due to a lower energy barrier. The bare COF is effective in generating $*CO_2$ and releasing *CO but less efficient in overall catalysis, mainly due to a high energy barrier in the $*CO_2$ to *COOH transition, a critical step in the process. Conversely, Co–COF displays superior photocatalytic activity as CoO integration significantly lowers this energy barrier, facilitating the reaction.

He et al. reported a $Ni(bpy)_3^{2+}$ complex supported on COFs synthesized via condensation of benzotrithiophene tricarbaldehyde with diethoxyterephthalohydrazide, dibutylterephthalohydrazide, and dihexylterephthalohydrazide (designated as BtE–COF, BtB–COF, and BtH–COF) that can enhance the photocatalytic CO_2RR.[40] These COFs, synthesized with varying alkyl chain lengths, showed distinct electron transport efficiencies. Notably, integrating $Ni(bpy)_3^{2+}$ into COFs markedly improved their photocatalytic performance. The strength of hydrogen bonds was found to be pivotal in facilitating electron transfer to the Ni complex. The standout performer was the BtE–COF with $Ni(bpy)_3^{2+}$, achieving a CO production of 2900 $\mu mol\,g^{-1}$ in 4 h, with an 88% selectivity for CO over H_2. This preference occurs probably due to weak heteroatom-hydrogen bonds (X···H–C, X=S, N, O), as seen in and similar bonds in two other $Ni(bpy)_3^{2+}$@COFs. Hydrogen bond strength decreases with longer alkyl chains in COFs. BtE–COF has the strongest hydrogen bonds, with a dominant N···H–C bond. Atomic dipole corrected Hirshfeld charges (ADCH) of Ni atoms in $Ni(bpy)_3^{2+}$@COFs follows the order: $Ni(bpy)_3^{2+}$@BtE–COF < $Ni(bpy)_3^{2+}$@BtB–COF < $Ni(bpy)_3^{2+}$@BtH–COF, correlating with hydrogen bond strength. The coordination structure of $Ni(bpy)_3^{2+}$ in BtE–COF was confirmed experimentally, forming a supramolecular system containing $Ni(bpy)_3^{2+}$. DFT calculations determined that the $Ni(bpy)_3^{2+}$ ion prefers to locate near the knot position in the COF, with confirmed weak interactions through heteroatom-hydrogen bonds. The diminution of steric groups on COF or metal complex can optimize catalytic performance, enhancing hydrogen bond interactions. The addition of Ni complex in the supramolecular system does not significantly change the growth kinetics of the excited state but facilitates decay kinetics, indicating efficient intermolecular electron transfer. The presence and distribution of Ni within the COF were confirmed using HAADF-STEM, which showed atomically dispersed Ni atoms. XPS and EXAFS further defined the chemical states and local coordination environment of Ni, primarily coordinating with nitrogen atoms. Stability assessments indicated that the materials are robust, maintaining their structure and chemical integrity post-reaction as evidenced by SEM, TEM, and XPS analyses, along with being thermally stable up to 350 °C. These methods collectively confirmed the effective integration and stability of the metal within the COF, supporting its potential in photocatalytic applications.

A DFT study by Xie et al. elucidated a Pt–COF photocatalytic system constructed by embedding Pt single atom in TFPT-TMT–COF (TFPT = tris(formylphenyl)triazine, TMT = trimethyltriazine) that can have an enhanced CO_2 photoreduction ability.[41] Pt can be effectively integrated into COF structures through N–Pt–C_2 linkages, resulting in a narrower band gap and enhanced light absorption. The Pt atom donates electrons to the COF, exhibiting an oxidation state, and its d orbitals, hybridized with the p orbitals of carbon and nitrogen, span the top of the valence band and the bottom of the conduction band. This Pt–COF shows a high CO_2 adsorption capacity with more negative adsorption energy, significantly activating CO_2 by elongating its C=O bonds and altering its linear structure. The key step in reducing CO_2 to CO on COF involves converting CO_2 to *COOH, which has an energy barrier of 1.41 eV. With Pt incorporation, this barrier drops significantly to 0.72 eV. However, further reduction of CO on Pt–COF faces a high barrier of 2.14 eV. These insights highlight the improved photocatalytic activity and selectivity for CO_2 reduction in COF photocatalysts with single Pt atoms (Figure 5).

The performance comparison of various M–COFs that can catalyze CO_2RR is summarized in Table S1 (SI).

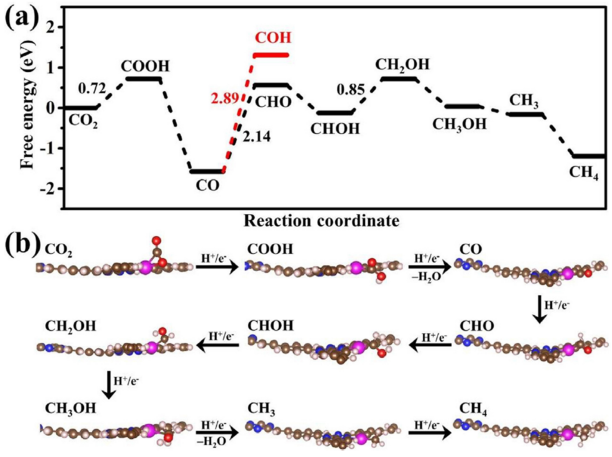

Figure 5. (a) Free energy diagram and (b) optimized structures for CO_2 reduction on Pt-loaded COF. Reprinted with permission from Ref. [41] Copyright 2023, Elsevier.

2.2. Oxygen Evolution Reaction

The process of splitting water electrochemically, especially the oxygen evolution reaction (OER), requires more energy compared to the hydrogen evolution reaction (HER). Interestingly, COFs that incorporate single metal site catalysts are becoming increasingly important in improving OER efficiency, especially in the context of water splitting. The distinct features of COFs, including their modifiable structures, robustness, lightweight nature, and porous composition, become particularly advantageous when paired with transition metals. This combination paves the way for the development of highly effective OER catalyst systems. Figure 6 shows various single-site metal-loaded COFs (M—COFs) used in OER reactions.

Gao et al. introduced a bimetallic Co–V COF (Co_xV_{1-x}@COF-SO_3) based on 2,5-diaminobenzenesulphonic and 2,4,6-triformylphloroglucinol (Figure 6a), achieving an OER overpotential of 300 mV at 10 mA·cm^{-2} in 1 M KOH, with superior performance in bimetallic forms, especially at a Co:V ratio of 0.5.[42] The metal incorporation was achieved through a cation-exchange strategy, with a measured content of around 5.0 wt% using ICP-AES. The presence and coordination of metal ions within the COFs were verified by XRD and spectroscopic techniques such as solid-state NMR and FTIR, which identified metal-oxygen

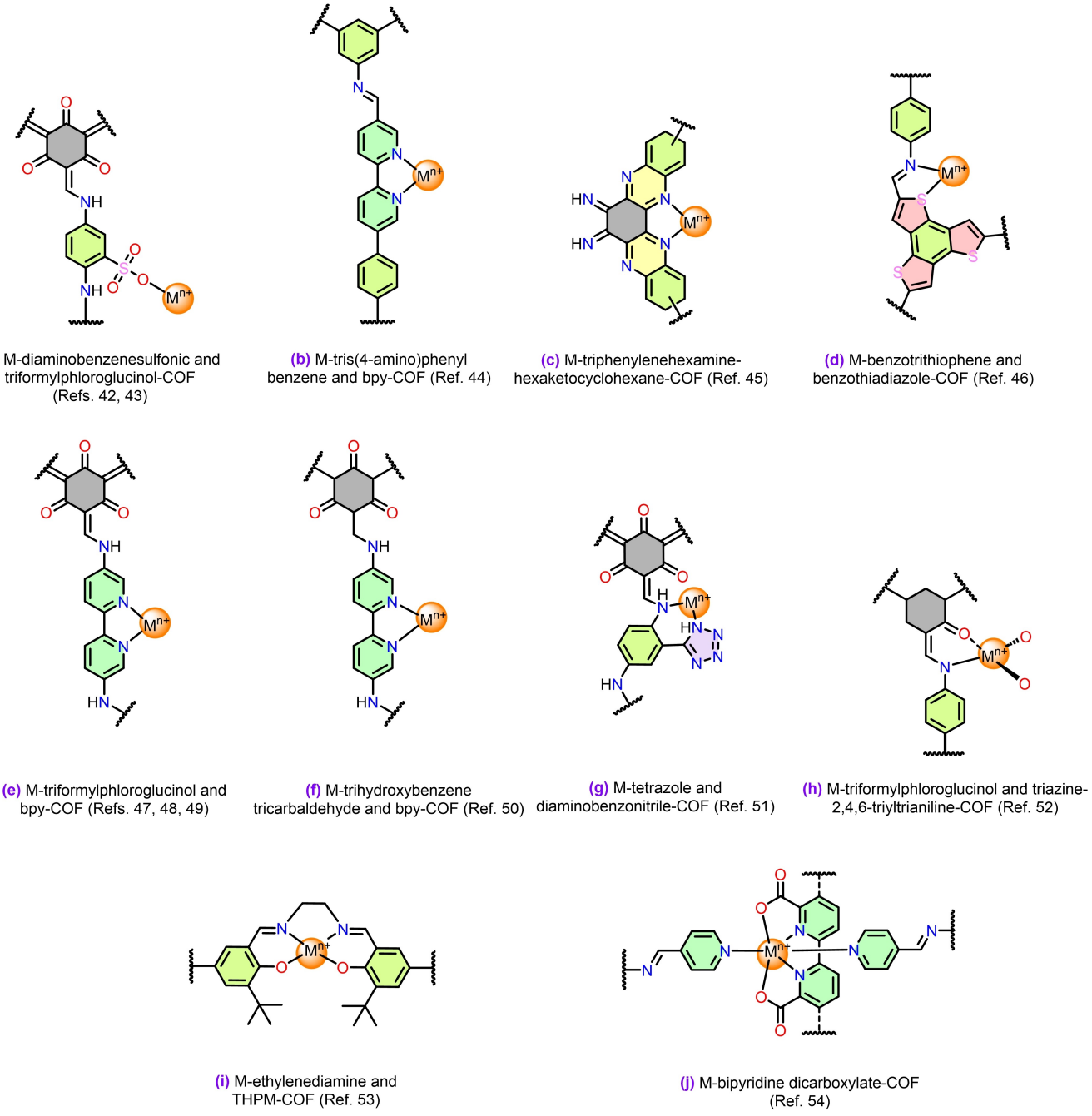

(a) M-diaminobenzenesulfonic and triformylphloroglucinol-COF (Refs. 42, 43)

(b) M-tris(4-amino)phenyl benzene and bpy-COF (Ref. 44)

(c) M-triphenylenehexamine-hexaketocyclohexane-COF (Ref. 45)

(d) M-benzotrithiophene and benzothiadiazole-COF (Ref. 46)

(e) M-triformylphloroglucinol and bpy-COF (Refs. 47, 48, 49)

(f) M-trihydroxybenzene tricarbaldehyde and bpy-COF (Ref. 50)

(g) M-tetrazole and diaminobenzonitrile-COF (Ref. 51)

(h) M-triformylphloroglucinol and triazine-2,4,6-triyltrianiline-COF (Ref. 52)

(i) M-ethylenediamine and THPM-COF (Ref. 53)

(j) M-bipyridine dicarboxylate-COF (Ref. 54)

Figure 6. Single-site metal-loaded COFs used in OER reactions. n = 0, 1, 2, etc.

bond formations indicative of successful metal integration. Stability assessments demonstrated the COFs' robustness and chemical stability under operational conditions, particularly their ability to undergo reversible transitions between catalysis-active and catalysis-inert phases through controlled metal ion removal and re-incorporation, proved the frameworks' suitability for repetitive use in catalytic applications without performance degradation. Another bimetallic COF incorporating Fe(II) and Ni(II) based on the same COF framework as the previous one (Figure 6a) was reported by the same group to achieve 308 mV at 10 mA·cm^{-2} and a TOF of 0.14 s^{-1} in 1 M KOH.[43] DFT, PXRD, FTIR, and XPS confirm the successful incorporation and coordination of metal ions within the COFs. These materials demonstrate robust structural stability and maintain high catalytic performance under operational conditions, as evidenced by extended chronoamperometric testing, making them promising for electrocatalytic applications.

Chen et al. introduced a Co(II) bipyridine-tris(4-aminophenyl) benzene-based COF (Figure 6b), demonstrating water oxidation under visible light (420 nm) at 152 μmol g^{-1} h^{-1}.[44] Co^{2+} is integrated as co-catalysts, primarily coordinating with bipyridine units rather than the imine groups, as evidenced by unchanged FTIR –C=N vibration peaks, XPS showing Co^{2+} presence, and NEXAFS spectra confirming Co integration. The COFs exhibit robust thermal stability up to 400 °C and maintain chemical integrity under photocatalytic conditions, although some decrease in crystallinity post-photocatalysis suggests structural degradation that may affect long-term stability.

Zhang et al. explored the OER catalytic performance of metals on triphenylenehexamine and hexaketocyclohexane-based COF supports (Figure 6c).[45] They identified metal-free COFs with sp^2-hybridized C4 sites as ideal for OER. Theoretical and experimental studies showed that Rh, Ni, Co, Fe, and Mn-enhanced COFs outperform the metal-free variant. Specifically, Co–COF (1:1 ratio to bare COF) reduced overpotential to 280 mV and doubled the current density to 399 mA·cm^{-2}. Ni–COF also reduced overpotential to 307 mV. Co–COF, Ni–COF, and Fe–COF showed lower overpotentials than bare COF, while Mn–COF and Cu–COF exhibited higher overpotentials, validating theoretical predictions and highlighting the potential of COF-based single-atom catalysts in OER enhancement.

He et al. reported a Co-loaded benzotrithiophene and benzothiadiazole COF (Co–BTB–COF, Figure 6d) capable of photocatalytically oxidizing water at a rate of 212 μmol L^{-1} h^{-1}.[46] The process features thermodynamically favourable water adsorption at a chelated Co site. The rate-limiting step involves forming an [Co–OH] intermediate from water, followed by oxidative dehydrogenation to [Co–O] and intermolecular water attack, resulting in O_2 production. Hydration during O_2 evolution reduces the energy barrier from 61.0 to 54.7 kcal·mol^{-1}, enhancing water oxidation efficiency and balancing the 4-electron pathway energy barrier (Figure 7). The M–COF incorporates atomically chelated cobalt (Co) sites critical for photocatalytic water oxidation. These metal sites were experimentally confirmed using HAADF-STEM, which showed the atomic distribution of Co, and XPS, which verified the

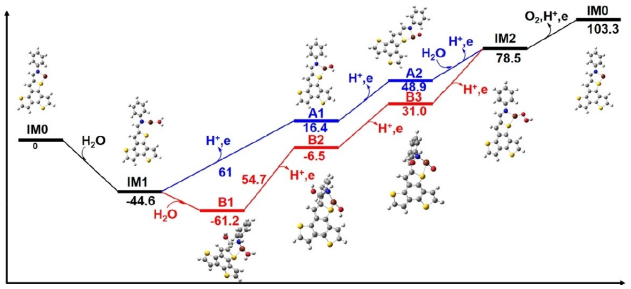

Figure 7. Gibbs energy profile for OER from water oxidation over Co-BtB–COF. IM1, IM2, A1, and A2 stand for [Co–OH_2], [Co-OOH], [Co–OH], and [Co–O], respectively. B1, B2, and B3 stand for hydrated [Co–OH_2], [Co–OH], and [Co–O], respectively. Reprinted with permission from Ref. [46]. Copyright 2023, American Chemical Society.

unique binding energies associated with the Co sites within the COF. Stability assessments revealed that the COF is thermally stable up to 500 °C. However, long-term photocatalytic activity led to a partial loss of crystallinity, as evidenced by changes in the PXRD patterns, though the material continued to show significant photocatalytic activity over repeated cycles.

The groundwork in this field was laid by Aiyappa et al. in 2016 with a triformylphloroglucinol and bipyridine-based COF integrated with Co(II) (Co-TpBpy, Figure 6e), showcasing OER proficiency in neutral pH.[47] This hybrid COF exhibited remarkable stability (over 1000 cycles), a TOF of 0.23 s^{-1}, a Faradaic efficiency of 95 %, and an overpotential of 400 mV at 1 mA·cm^{-2} current density. The Co-TpBpy contains about 12–13 % cobalt by weight, confirmed via TGA and ICP analyses. Structural integrity and cobalt modification are validated through PXRD, which shows no extraneous peaks, and UV-vis and XPS, indicating Co's successful coordination with the framework's nitrogen atoms. The material maintains a significant surface area crucial for catalytic activity, as shown by N_2 adsorption isotherms. Electrochemical tests reveal exceptional stability, with Co-TpBpy retaining 94 % of its activity after 1000 cycles and showing negligible Co leaching, underscoring its durability and efficacy in water oxidation processes. Wu and team escalated the research with a bimetallic COF (trihydroxybenzene-bipyridine with Fe(II) and Co(II), Figure 6e), surpassing its predecessor in OER activity and pH resilience, achieving overpotentials of 370 mV in 1 M KOH and 360 mV in 0.5 M H_2SO_4.[48] Metal loading was quantified using ICP-OES, which showed an increase in metal content post-carbonization with Fe and Co contents rising to 8.2 % and 10.5 %, respectively. Experimental confirmation of metal binding sites was achieved through XPS and HRTEM, indicating successful integration of metals into the COF structure. Stability assessments via TGA and electrochemical testing demonstrated that the bimetallic COF retains nearly 100 % of its original current density over extended use, showcasing its durability and superior methanol tolerance compared to conventional Pt/C catalysts.

Zhao et al. reported a Co-based COF (Figure 6e), reaching an OER overpotential of 380 mV at 10 mA·cm^{-2} in 0.1 M KOH.[49] Co is loaded by soaking the framework in cobalt acetate, achieving an atomic cobalt concentration of 2.84 %. The metal

binding is confirmed through XPS, which shows characteristic Co–N bonds and the presence of Co^{2+} states, and XAS which indicates the oxidation state and local coordination environment. The framework demonstrates robust stability, maintaining its structural integrity and catalytic performance even after prolonged operational testing, showcasing its potential for efficient and durable electrocatalysis.

Liu et al. reported a bipyridine-based, bimetallic COF with Fe(III) and Co(II) (Figure 6f), showing 331 mV overpotential and 1000-cycle stability in 1 M KOH,[50] with optimal performance at a Co:Fe ratio of 3:1. Metal binding sites within the COFs were confirmed using techniques like XPS and PXRD, which demonstrated the preservation of crystal structures and the presence of metal elements post-modification. The stability and functionality of the metal-loaded COFs were validated through CV tests and nitrogen adsorption measurements, showing good stability and a decrease in surface area and pore size, indicating changes in porosity that may impact their utility in applications like electrocatalysis. These analyses confirm the successful integration and stability of metals within the COF structures. Similarly, Liang et al. reported a tetrazole functionalized COF based on 1,3,5-triformylphloroglucinol and 2,5-diaminobenzonitrile with Co(II) (Figure 6g), achieving 390 mV OER overpotential at 10 $mA{\cdot}cm^{-2}$ and maintaining stability for 1000 cycles in 1 M KOH.[51]

Wang et al. introduced single-atom iron catalysts in COFs with Fe–NO coordination, based on triformylphloroglucinol and triazine-2,4,6-triyltrianiline (Figure 6h), achieving 290 mV electrocatalytic OER potential in 1 M KOH.[52] DFT calculations indicated lower ΔG for the potential-determining step in this COF compared to the Ni-variant (Figure 8). The report details the metal loading to be about 1.0 wt% for Fe and Ni samples. Experimental confirmation of the metal binding sites was achieved using XAFS and wavelet transforms, confirming the atomic dispersion and specific coordination of these metals without metal-metal bonding. Additionally, the materials demonstrated exceptional stability during extended OER, maintaining structural and electronic integrity, as evidenced by various spectroscopic and microscopic analyses.

Zhou et al. developed bivalent transition metal-loaded COFs with ethylenediamine and 5,5′,5″,5‴-((methanetetrayltetrakis(benzene-4,1-diyl))tetrakis(ethyne-2,1-diyl))tetrakis(3-tertbutyl)-2-hydroxybenzaldehyde (THPM) ligands (Figure 6i), finding Ni–COF to be most efficient at 10 $mA{\cdot}cm^{-2}$, achieving 335 mV OER overpotential, followed by Co–COF (347 mV), Zn–COF (359 mV), Fe–COF (369 mV), and Cu–COF (384 mV).[53] The metal content in various M–COFs was quantified using ICP, showing, for example, about 5.6 wt% nickel in Ni–COF. The structural integration and metal binding sites within these frameworks were confirmed through techniques such as XANES, EXAFS, FTIR, and solid-state NMR. These analyses demonstrated the presence of Ni-N_2O_2 moieties specifically in Ni–COF. Additionally, the materials' stability was evaluated under electrochemical conditions for OER, where Ni–COF showed operational stability over 65 h at a consistent current density and thermal stability tests indicated that M–COFs could withstand temperatures up to at least 200 °C, evidenced by TGA. Karak et al. introduced a Ru and bipyridine dicarboxylate ligand-based COF (Figure 6j), marking a breakthrough in photocatalytic OER with a rate of ~26,000 $\mu mol\,L^{-1}\,s^{-1}$.[54] This COF 3D structure facilitated water molecule activation through two highly oxidized Ru-oxyl radicals. Metal loading is achieved through a condensation reaction between a dialdehyde and a tetraamine, creating an imine-linked network that fully incorporates Ru centers, as confirmed by CP-MAS ^{13}C NMR and FTIR spectroscopy. Structural integrity and metal binding sites are further verified using PXRD and SEM, which illustrate the material's crystalline nature and nanoscale morphology. Stability assessments, including multiple catalytic cycles and thermogravimetric analysis, dem-

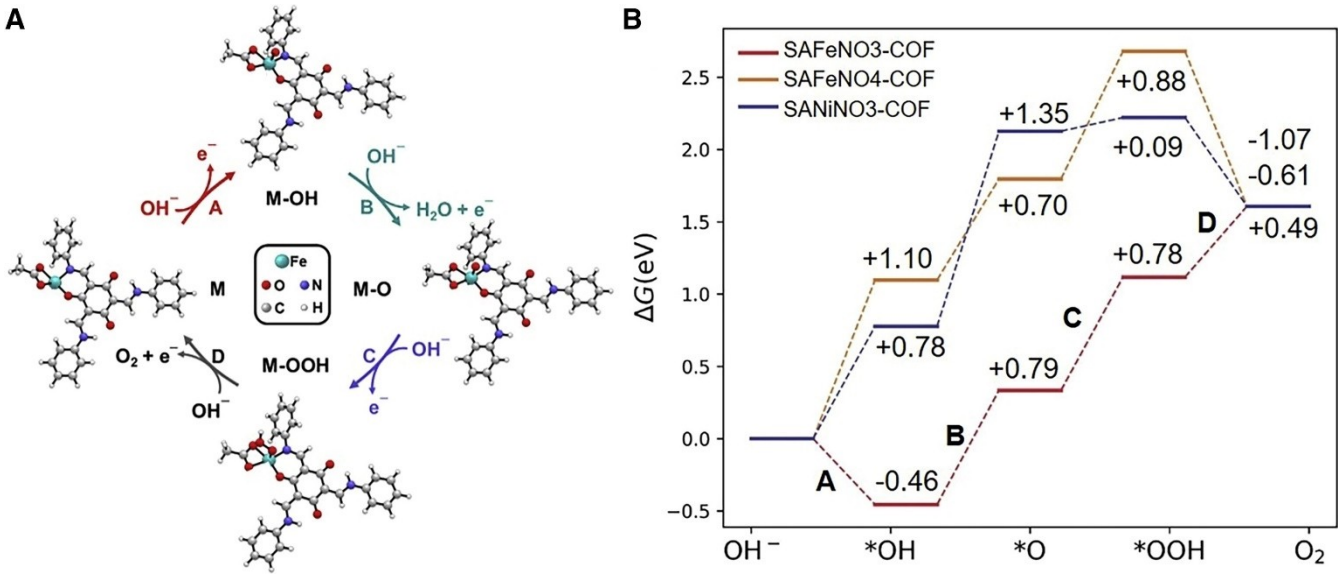

Figure 8. DFT calculations for (a) the catalytic OER mechanism cycles of the Fe-SAC cluster model, and (b) the OER volcano plot of the overpotential η versus $\Delta G_O - \Delta G_{OH}$ for the Fe-NO3 (Fe-SAC@COF), Ni-NO3 (Ni-SAC@COF), and Fe-NO4 models. Reprinted with permission from Ref. [52]. Copyright 2022, Elsevier.

onstrate the material's robustness, with the crystalline COF showing superior thermal stability and consistent catalytic activity under various conditions.

Barlocco et al. conducted a computational study of single-atom catalysts with 3d, 4d, and 5d transition metals for OER.[55] They found that Fe, Co, Ir, and Rh-containing COFs excelled in OER simulations. Ti@COF and W@COF showed strong *OH binding, while Ir@COF, Rh@COF, Mn@COF, Fe@COF, and Co@COF had an ideal *OH binding free energy of ~1.2 eV. In contrast, Ni@COF, Pd@COF, and Pt@COF demonstrated lower reactivity due to large Gibbs energy (ΔG). *O intermediates also varied in reactivity, ranging from highly reactive (Ti@COF, W@COF) to more inert (Ni@COF, Pd@COF, Pt@COF), indicating diverse catalytic properties. The authors outline computed metal binding sites within a COF, which offers superior binding energies for transition metals due to its specialized cavities. For example, Co demonstrates a notable binding energy of −9.27 eV in the COF, significantly more robust than the −7.79 eV and −3.34 eV seen with nitrogen-doped graphene and carbon nitride, respectively. Pt also exhibits a higher binding energy of −10.58 eV in COF, compared to −7.99 eV and −2.79 eV in the other two materials. This enhanced binding indicates that COFs create a highly stable environment for transition metals, effectively reducing diffusion and sintering, though this stability might also diminish the catalytic reactivity by overly stabilizing the metal sites. This work details single-atom catalysts stabilized by a COF, focusing on transition metals such as Ti, V, and Cr, among others, embedded within the COF structure. These metals are atomically dispersed and likely experimentally confirmed to be coordinated with nitrogen atoms in the COF, akin to structures found in nitrogen-doped graphene and porphyrins. This configuration enhances the catalytic properties and stability of the metals, preventing issues like sintering by maintaining strong metal binding energies. The stability is further supported by computational studies evaluating the thermodynamic stability of various reaction intermediates, making these materials promising for applications like hydrogen and oxygen evolution reactions.

The performance comparison of various M—COFs that can catalyze OER is collected in Table S2 (SI).

2.3. Organic Transformations

Another important area of interest concerns the use of single atoms in COFs for organic transformations,[56] which are typically catalyzed in homogeneous phases. The COF supports may play a synergistic role in the reaction, making the heterogeneous system more efficient than the homogeneous counterpart. Selected recent examples highlighting the active sites and the reaction mechanisms from both experimental and computational points of view are surveyed as follows.

Han et al. prepared an imine-based 2D COF loaded with Pd(II) for the oxidative Heck reaction between phenylboronic esters and aliphatic alkenes.[57] The $Pd(OAc)_2$ fragments bind to N and OH groups within the same layer (Figure 9a). Using 1-octene as a test case, they found that the Pd–COF systems

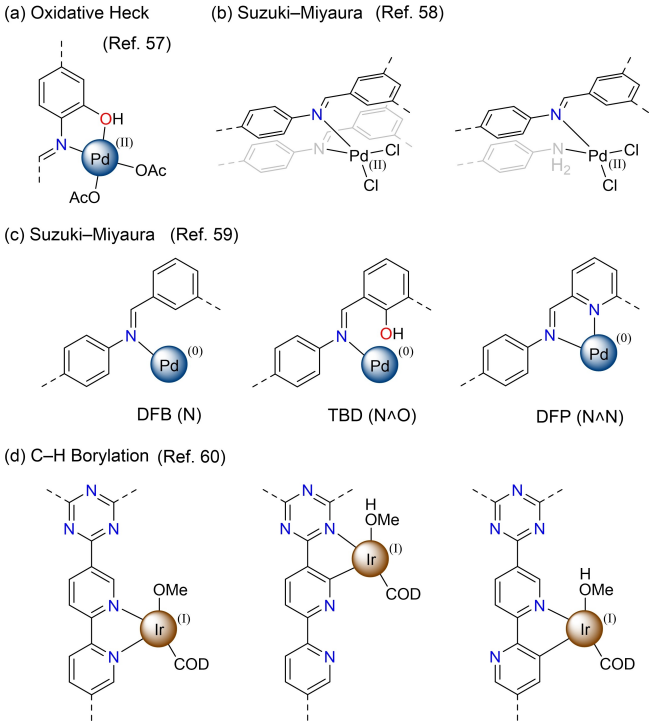

Figure 9. Single-atom sites anchored to several COF supports for selected organic transformations.

provided a linear:branched ratio of 50:1, while the $Pd(OAc)_2$ catalyst only produced a ratio of 5:1. The same selectivity trend was found for a large scope of alkenes. The heterogeneous system was reused up to nine times with minor loss of Pd (from 5.13% to 4.97% by ICP). Interestingly, traces of the Cu(II) reactant were found in the framework. To support the selectivity results, they performed DFT calculations on a cluster model of the Pd–COF. In line with experiments, they found that the transition state for the linear product was 2.7 kcal·mol^{-1} lower in Gibbs energy than that for the branched one.

Romero-Muñiz et al. reported an imine-based 2D COF, containing local defects, which incorporated Pd(II) sites via in situ metalation and gel metalation.[58] The resulting materials were active for the Suzuki–Miyaura reaction between aryl halides and phenylboronic acid as substrates. To probe the local environment of Pd(II) within the COF, they performed a combined experimental-computational approach. Before catalysis, EXAFS data provided clear signals corresponding to Pd–N and Pd–Cl, and XANES data pointed to a Pd(II) oxidation state. After catalysis, in EXAFS the Pd–N signal remained but the Pd–Cl ones were exchanged by Pd–Br, while in XANES a small shift towards Pd(0) was observed, in line with the detection of NPs via TEM. As for computational studies, periodic DFT calculations evaluated the coordination of a $[Pd(Cl)_2]$ unit to defect-free and defective materials, the latter resulting from imine hydrolysis. The Pd center adopted a square-planar geometry and coordinated to different COF layers via two imines for defect-free and one imine and one amine for defective (Figure 9b). Both types of sites are energetically accessible (within 3 kcal·mol^{-1}) and thus potentially relevant for

catalysis, although the defective one is favoured when increasing the number of defects.

Krishnaraj et al. studied a series of imine-based 2D COFs containing N, N∧O, and N∧N as available coordination sites for Pd(II) atoms.[59] The resulting COFs were not fully crystalline according to the broad PXRD patterns observed. The metal-loaded materials DFB (N), TBD (N∧O), and DFP (N∧N) (Figure 9c) were active for the Suzuki–Miyaura reaction between bromobenzaldehyde and phenylboronic acid in the presence of K_2CO_3 at 150 °C. High yields with complete conversions were obtained for the catalysts after 2, 4, and 16 h, respectively. The different kinetics can be explained via several observations. Firstly, the slow reaction for DFP (N∧N) was attributed to the initial formation of Pd(0) active species via homocoupling of phenylboronic acids. Experiments readily yielded biphenyl products for DFB (N) and TBD (N∧O), while an induction period was observed for DFP (N∧N). DFT studies on cluster models supported these results, as the formation of Pd(0) in DFP (N∧N) was endothermic by 8.0 kcal·mol^{-1}. To provide further details, the reaction mechanism (oxidative addition, transmetalation, and reductive elimination) was computed at the DFT level using cluster models of each catalyst (Figure 10). Similar reaction profiles with low energy barriers (*ca.* 13 kcal·mol^{-1}) were obtained. Secondly, the fast reaction for DFB (N) was attributed to partial Pd leaching observed through the hot filtration test, as the homogeneous reaction with $Pd(OAc)_2$ also required a short time of 1 h. No leaching was observed for TBD (N∧O) and DFP (N∧N), indicating the stronger coordination environment of these two COF supports.

Tahir et al. synthesized a low-crystalline triazine-based COF containing bpy sites for the anchoring of Ir(I) using the precursor $[Ir(OMe)(COD)_2]$ (COD = cycloocta-1,5-diene).[60] The resulting material was active for the Ir-catalyzed C–H borylation of aromatic compounds with $B_2(pin)_2$. The precise coordination environment of Ir(I) was studied via DFT calculations on a cluster model. They evaluated one isomer coordinated to the bpy unit and two cyclometalated isomers bound to triazine and bpy units, respectively (Figure 9d). The two structures involving bpy were isoenergetic, but the latter was discarded after additional simulations that included BPIN. A related system also based on Ir was later reported for aerobic oxidation reactions of alcohols.[61] The metal unit [Ir(III)Cp*Cl]Cl was anchored to bpy moieties (as in Figure 9d) and performed better than its homogeneous counterpart. This was attributed to a synergistic effect between the COF support, which activates oxygen and the alcohol, and the Ir centre, which can adsorb the activated substrate.

Gutiérrez et al. prepared an imine-based 2D COF with bpy moieties which were metalated with the $CoCl_2$ precursor as confirmed by EXAFS and DFT.[62] The resulting material was then reduced *in situ* to provide Co(0) active sites for olefin hydroboration. During this process, imine linkages were also reduced to amines according to FTIR. Although the material lost some crystallinity, the connectivity remained the same. The presence of the COF as a solid matrix was key to avoiding any deactivation pathways, such as dimerization, disproportionation, or aggregation (Figure 11a). Mechanistic studies were performed on the Co–COF-catalyzed model reaction between 1-octene and pinacolborane (HBpin) at room temperature. Deuterium labelling experiments showed a fast isomerization from 1-octene to 2-octene and other internal alkenes via chain walking, although the hydroboration reaction was highly selective toward terminal ones. Kinetic studies suggested a first-order rate dependence for the catalyst and nearly zero-order rate dependence for the olefin and the borane. DFT simulations on a cluster model provided a general picture of the reaction mechanism between HBpin and 1-pentene, which involved oxidative boryl migration, isomerization, and reductive elimination. The Gibbs energy profile on the doublet surface is shown

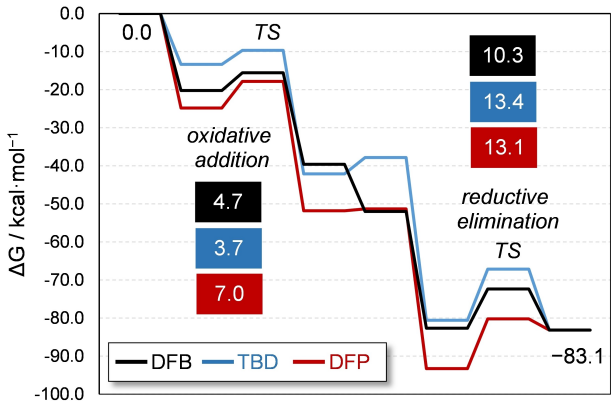

Figure 10. Gibbs energy profiles for the Suzuki-Miyaura reaction catalyzed by Pd(0) sites at three different COFs (Ref. [59]).

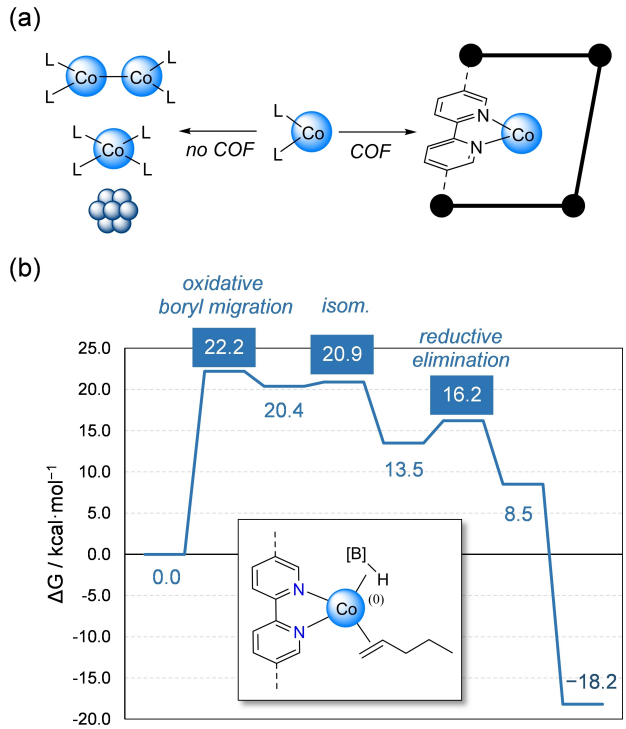

Figure 11. (a) Preventing disproportionation, dimerization and aggregation of homogeneous organometallic catalysts using COF supports and (b) Gibbs energy profile for the hydroboration of 1-pentene catalyzed by Co(0) sites at COFs (Ref. [62]).

in Figure 11b. The almost-concerted process with an energy barrier of *ca.* 22 kcal·mol^{-1} agrees with the experimental observations. Finally, computed spin densities pointed to 1-electron processes with a redox-active COF.

Jia et al. reported a cobalt-containing 2D COF as a dual photoredox catalyst for the visible-light-driven C–H annulation of amides with alkynes.[63] The imine-based COF had bpy units to anchor the metal, which was introduced using the Co-$(OAc)_2 \cdot 4H_2O$ precursor. Several experiments were carried out to characterize the active site: TEM confirmed that no metal nanoparticles were formed, XANES indicated a Co(II) oxidation state, and EXAFS pointed to Co–N coordination modes, although no further details were provided to discern between imine and bpy N atoms. As for the reaction mechanism, ESR spectra showed the formation of singlet oxygen $^1O_2$ via energy transfer, which is tentatively involved in the initial oxidation of Co(II) to Co(III). Additional deuterium-labelling experiments suggested that the C–H bond activation could be irreversible but not rate-determining.

3. Summary and Outlook

Covalent organic frameworks have become crucial solid supports for single-atom metal catalysts, thus bridging the gap between homogeneous and heterogeneous worlds. Typical synthetic methods involve a direct metalation during COF synthesis or a post-synthetic metalation of the COF. Such approaches allow for a controlled installation of metal atoms, giving rise to a rational design of well-defined catalytic sites. These hybrid materials may present catalytic advantages on several fronts, such as enhanced activity, tunable selectivity, reduced deactivation, and reliable recyclability.

Synthetic methods allow for the incorporation of well-defined metal sites into the COF cavity, influencing the thermodynamics and kinetics of the reactions. Those metal sites in the COFs can be rationally tuned to explore COF properties directly resulting from the framework structure, like electrical conductivity, mechanical strength, thermal stability, or substrate transport. For example, it has been proposed that mechanical constraint, locks and isolates catalytic sites within the structure, limiting bimolecular decomposition pathways of highly reactive species, enhancing reactivity and chemical stability when compared with homogeneous counterparts. The electrical conductivity in COFs yields higher electrocatalytic current densities, while the right selection of donor-acceptor COF's subunits can improve charge dynamics, and carrier separation, increasing photocatalytic efficiency. Such as the 3D reticular structure of COFs enables high catalytic loadings and density of sites on electrodes, increasing catalytic current densities, and durability. While their insolubility facilitates recycling. Moreover, precise control over the distribution of catalytic sites is crucial for cascade reactions and selective chemical processes. Lastly, the high surface area and porosity of COFs facilitate gas adsorption, which can be exploited in the transformation of gases like CO_2 reduction, highlighting their value in environmental and energy-related applications.

While synthesis and applications are well reported, less is known about their unique reaction mechanisms. Here we have highlighted the key mechanistic features of these complex materials for selected photo-, electro- and thermal-based processes. In the future, we encourage a deeper investigation of the potential non-innocent role of COFs at both experimental and computational levels. Such a strategy would lead us to promote and even design synergies between support and single-atom catalysts.

Acknowledgements

This work has received financial support from MCIN/ AEI/ 10.13039/501100011033 (PID2020-119116RA-I00, M.A.O.), Xunta Distinguished Researcher program (ED431H 2020/21), the Xunta de Galicia (Centro singular de investigación de Galicia acreditacion 2019–2022, ED431G 2019/03) and the European Union (European Regional Development Fund - ERDF). A.G. acknowledges the funding from the European Union's Horizon Europe research and innovation programme under the Marie Skłodowska-Curie grant agreement No.101105451. The authors also acknowledge the financial support of the ICIQ Foundation, the CERCA Program/Generalitat de Catalunya, MCIN through Severo Ochoa Excellence Accreditation 2020–2023 (CEX2019-000925-S, MIC/AEI), AGAUR (2021 SGR 01260), MCIN (PID2019-110050RB-I00, J.L-F.; PDC2022-133451-I00, J.L-F., PID2022-140142OB-I00) and "la Fundación Ramón Areces" (ElectroFuel).

Conflict of Interests

The authors declare no conflict of interest.

Keywords: COF · reaction mechanisms · single metal site · CO_2RR · OER

[1] R. Freund, S. Canossa, S. M. Cohen, W. Yan, H. Deng, V. Guillerm, M. Eddaoudi, D. G. Madden, D. Fairen-Jimenez, H. Lyu, L. K. Macreadie, Z. Ji, Y. Zhang, B. Wang, F. Haase, C. Wöll, O. Zaremba, J. Andreo, S. Wuttke, C. S. Diercks, *Angew. Chem. Int. Ed.* **2021**, *60*, 23946–23974.
[2] X. Feng, X. Ding, D. Jiang, *Chem. Soc. Rev.* **2012**, *41*, 6010–6022.
[3] C. S. Diercks, O. M. Yaghi, *Science* **2017**, *355*, eaal1585.
[4] M. S. Lohse, T. Bein, *Adv. Funct. Mater.* **2018**, *28*, 1705553.
[5] K. Geng, T. He, R. Liu, S. Dalapati, K. T. Tan, Z. Li, S. Tao, Y. Gong, Q. Jiang, D. Jiang, *Chem. Rev.* **2020**, *120*, 8814–8933.
[6] J. Guo, D. Jiang, *ACS Cent. Sci.* **2020**, *6*, 869–879.
[7] Z. Alsudairy, N. Brown, A. Campbell, A. Ambus, B. Brown, K. Smith-Petty, X. Li, *Mater. Chem. Front.* **2023**, *7*, 3298–3331.
[8] Y. Zhi, Z. Wang, H.-L. Zhang, Q. Zhang, *Small* **2020**, *16*, 2001070.
[9] J. Artz, *ChemCatChem* **2018**, *10*, 1753–1771.
[10] A. Iemhoff, M. Vennewald, R. Palkovits, *Angew. Chem. Int. Ed.* **2023**, *62*, e202212015.
[11] J. L. Segura, S. Royuela, M. M. Ramos, *Chem. Soc. Rev.* **2019**, *48*, 3903–3945.
[12] S. M. J. Rogge, A. Bavykina, J. Hajek, H. Garcia, A. I. Olivos-Suarez, A. Sepúlveda-Escribano, A. Vimont, G. Clet, P. Bazin, F. Kapteijn, M. Daturi, E. V. Ramos-Fernandez, F. X. Llabrés i Xamena, V. Van Speybroeck, J. Gascon, *Chem. Soc. Rev.* **2017**, *46*, 3134–3184.
[13] Q. Guan, L.-L. Zhou, Y.-B. Dong, *Chem. Soc. Rev.* **2022**, *51*, 6307–6416.
[14] H. Salemi, M. Debruyne, V. Van Speybroeck, P. Van Der Voort, M. D'hooghe, C. V. Stevens, *J. Mater. Chem. A* **2022**, *10*, 20707–20729.

[15] S. Daliran, A. R. Oveisi, Y. Peng, A. López-Magano, M. Khajeh, R. Mas-Ballesté, J. Alemán, R. Luque, H. Garcia, *Chem. Soc. Rev.* **2022**, *51*, 7810–7882.
[16] G.-B. Wang, S. Li, C.-X. Yan, F.-C. Zhu, Q.-Q. Lin, K.-H. Xie, Y. Geng, Y.-B. Dong, *J. Mater. Chem. A* **2020**, *8*, 6957–6983.
[17] A. López-Magano, S. Daliran, A. R. Oveisi, R. Mas-Ballesté, A. Dhakshinamoorthy, J. Alemán, H. Garcia, R. Luque, *Adv. Mater.* **2023**, *35*, 2209475.
[18] D. Ma, Y. Wang, A. Liu, S. Li, C. Lu, C. Chen, *Catalysts* **2018**, *8*, 404.
[19] D. Rodríguez-San-Miguel, C. Montoro, F. Zamora, *Chem. Soc. Rev.* **2020**, *49*, 2291–2302.
[20] M. Chen, H. Li, C. Liu, J. Liu, Y. Feng, A. G. H. Wee, B. Zhang, *Coord. Chem. Rev.* **2021**, *435*, 213778.
[21] A. Schlachter, P. Asselin, P. D. Harvey, *ACS Appl. Mater. Interfaces* **2021**, *13*, 26651–26672.
[22] S. Lin, C. S. Diercks, Y.-B. Zhang, N. Kornienko, E. M. Nichols, Y. Zhao, A. R. Paris, D. Kim, P. Yang, O. M. Yaghi, C. J. Chang, *Science* **2015**, *349*, 1208–1213.
[23] S. Huang, K. Chen, T.-T. Li, *Coord. Chem. Rev.* **2022**, *464*, 214563.
[24] L. Feng, K.-Y. Wang, E. Joseph, H.-C. Zhou, *Trends Chem.* **2020**, *2*, 555–568.
[25] M. Lu, Q. Li, J. Liu, F.-M. Zhang, L. Zhang, J.-L. Wang, Z.-H. Kang, Y.-Q. Lan, *Appl. Catal. B* **2019**, *254*, 624–633.
[26] W. Zhong, R. Sa, L. Li, Y. He, L. Li, J. Bi, Z. Zhuang, Y. Yu, Z. Zou, *J. Am. Chem. Soc.* **2019**, *141*, 7615–7621.
[27] S. Das, P. Sarkar, M. Goswami, S. M. Ali, M. R. Mollah, S. M. Islam, *Mater. Chem. Front.* **2023**, *7*, 3349–3364.
[28] Y.-Z. Cheng, W. Ji, P.-Y. Hao, X.-H. Qi, X. Wu, X.-M. Dou, X.-Y. Bian, D. Jiang, F.-T. Li, X.-F. Liu, D.-H. Yang, X. Ding, B.-H. Han, *Angew. Chem. Int. Ed.* **2023**, *62*, e202308523.
[29] Y. Zhang, L. Cao, G. Bai, X. Lan, *Small* **2023**, *19*, 2300035.
[30] Z. Fu, X. Wang, A. M. Gardner, X. Wang, S. Y. Chong, G. Neri, A. J. Cowan, L. Liu, X. Li, A. Vogel, R. Clowes, M. Bilton, L. Chen, R. S. Sprick, A. I. Cooper, *Chem. Sci.* **2020**, *11*, 543–550.
[31] T. W. Schneider, M. Z. Ertem, J. T. Muckerman, A. M. Angeles-Boza, *ACS Catal.* **2016**, *6*, 5473–5481.
[32] G. C. Dubed Bandomo, S. S. Mondal, F. Franco, A. Bucci, V. Martin-Diaconescu, M. A. Ortuño, P. H. Van Langevelde, A. Shafir, N. López, J. Lloret-Fillol, *ACS Catal.* **2021**, *11*, 7210–7222.
[33] G. C. Dubed Bandomo, F. Franco, C. Liu, S. S. Mondal, A. Gallo, C. Nervi, J. Lloret-Fillol, *ACS Appl. Energ. Mater.* **2024**, *7*, 1348–1357.
[34] L. Zou, Z.-A. Chen, D.-H. Si, S.-L. Yang, W.-Q. Gao, K. Wang, Y.-B. Huang, R. Cao, *Angew. Chem.* **2023**, *135*, e202309820.
[35] J. Qiu, Y. Zheng, L. Wang, M. Liu, L. Tian, X. Yu, X. An, G. Lv, *J. Mater. Chem. A* **2023**, *11*, 4572–4578.
[36] S. Yang, R. Sa, H. Zhong, H. Lv, D. Yuan, R. Wang, *Adv. Funct. Mater.* **2022**, *32*, 2110694.
[37] Y. Yang, H.-Y. Zhang, Y. Wang, L.-H. Shao, L. Fang, H. Dong, M. Lu, L.-Z. Dong, Y.-Q. Lan, F.-M. Zhang, *Adv. Mater.* **2023**, *35*, 2304170.
[38] L. Zhu, Z. Liang, H. Li, Q. Xu, D. Jiang, H. Du, C. Zhu, H. Li, Z. Lu, Y. Yuan, *Small* **2023**, *19*, 2301017.
[39] L.-Y. Ai, Q. Wang, X.-W. Chen, G.-F. Jiang, *J. Chem. Eng.* **2023**, *475*, 146106.
[40] Y. He, Y. Zhao, X. Wang, Z. Liu, Y. Yu, L. Li, *Angew. Chem.* **2023**, *135*, e202307160.
[41] F. Xie, C. Bie, J. Sun, Z. Zhang, B. Zhu, *J. Mater. Sci. Technol.* **2024**, *170*, 87–94.
[42] Z. Gao, Z. Yu, Y. Huang, X. He, X. Su, L. Xiao, Y. Yu, X. Huang, F. Luo, *J. Mater. Chem. A* **2020**, *8*, 5907–5912.
[43] Z. Gao, L. L. Gong, X. Q. He, X. M. Su, L. H. Xiao, F. Luo, *Inorg. Chem.* **2020**, *59*, 4995–5003.
[44] J. Chen, X. Tao, C. Li, Y. Ma, L. Tao, D. Zheng, J. Zhu, H. Li, R. Li, Q. Yang, *Appl. Catal. B* **2020**, *262*, 118271.
[45] R. Zhang, W. Liu, F.-M. Zhang, Z.-D. Yang, G. Zhang, X. C. Zeng, *Appl. Catal. B* **2023**, *325*, 122366.
[46] Y. He, G. Liu, Z. Liu, J. Bi, Y. Yu, L. Li, *ACS Energy Lett.* **2023**, *8*, 1857–1863.
[47] H. B. Aiyappa, J. Thote, D. B. Shinde, R. Banerjee, S. Kurungot, *Chem. Mater.* **2016**, *28*, 4375–4379.
[48] D. Wu, Q. Xu, J. Qian, X. Li, Y. Sun, *Chem. Eur. J.* **2019**, *25*, 3105–3111.
[49] X. Zhao, P. Pachfule, S. Li, T. Langenhahn, M. Ye, C. Schlesiger, S. Praetz, J. Schmidt, A. Thomas, *J. Am. Chem. Soc.* **2019**, *141*, 6623–6630.
[50] X. Liu, L. Feng, Y. Li, T. Xia, Z. Sui, Q. Chen, *Molecules* **2022**, *27*, 5193.
[51] Y. Liang, T. Xia, Z. Wu, Y. Yang, Y. Li, Z. Sui, C. Li, R. Fan, X. Tian, Q. Chen, *Mater. Today Chem.* **2022**, *24*, 100777.
[52] X. Wang, L. Sun, W. Zhou, L. Yang, G. Ren, H. Wu, W.-Q. Deng, *Cell Rep. Phys. Sci.* **2022**, *3*, 100804.
[53] W. Zhou, L. Yang, X. Wang, W. Zhao, J. Yang, D. Zhai, L. Sun, W. Deng, *JACS Au* **2021**, *1*, 1497–1505.
[54] S. Karak, V. Stepanenko, M. A. Addicoat, P. Keßler, S. Moser, F. Beuerle, F. Würthner, *J. Am. Chem. Soc.* **2022**, *144*, 17661–17670.
[55] I. Barlocco, G. D. Liberto, G. Pacchioni, *Energy Adv.* **2023**, *2*, 1022–1029.
[56] S. Abednatanzi, M. Najafi, P. Gohari Derakhshandeh, P. Van Der Voort, *Coord. Chem. Rev.* **2022**, *451*, 214259.
[57] J. Han, X. Sun, X. Wang, Q. Wang, S. Hou, X. Song, Y. Wei, R. Wang, W. Ji, *Org. Lett.* **2020**, *22*, 1480–1484.
[58] I. Romero-Muñiz, A. Mavrandonakis, P. Albacete, A. Vega, V. Briois, F. Zamora, A. E. Platero-Prats, *Angew. Chem. Int. Ed.* **2020**, *59*, 13013–13020.
[59] C. Krishnaraj, H. S. Jena, K. S. Rawat, J. Schmidt, K. Leus, V. Van Speybroeck, P. Van Der Voort, *ACS Appl. Mater. Interfaces* **2022**, *14*, 50923–50931.
[60] N. Tahir, F. Muniz-Miranda, J. Everaert, P. Tack, T. Heugebaert, K. Leus, L. Vincze, C. V. Stevens, V. Van Speybroeck, P. Van Der Voort, *J. Catal.* **2019**, *371*, 135–143.
[61] S. Abednatanzi, P. Gohari Derakhshandeh, P. Tack, F. Muniz-Miranda, Y.-Y. Liu, J. Everaert, M. Meledina, F. Vanden Bussche, L. Vincze, C. V. Stevens, V. Van Speybroeck, H. Vrielinck, F. Callens, K. Leus, P. Van Der Voort, *Appl. Catal. B: Environ.l* **2020**, *269*, 118769.
[62] L. Gutiérrez, V. Martin-Diaconescu, C. Casadevall, F. Oropeza, V. A. De la Peña O'Shea, J. Meng, M. A. Ortuño, J. Lloret-Fillol, *ACS Catal.* **2023**, *13*, 3044–3054.
[63] J. Jia, X. Bu, X. Yang, *J. Mater. Chem. A* **2022**, *10*, 11514–11523.

Manuscript received: January 16, 2024
Revised manuscript received: June 2, 2024
Accepted manuscript online: June 2, 2024
Version of record online: ■■, ■■

REVIEW

In this minireview, we survey and discuss the key mechanistic features of selected single metal site catalysts supported on covalent organic frameworks (COFs), with a focus on photo- and electrocatalytic CO_2 reduction, oxygen evolution reaction, and organic transformations.

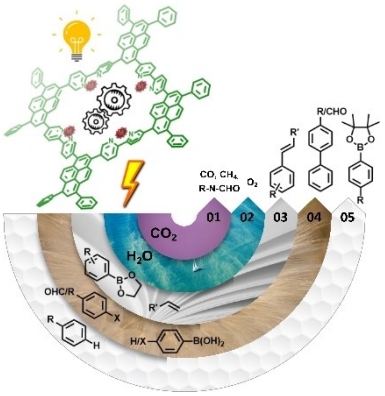

Dr. A. Gopakumar, Dr. M. A. Ortuño, Prof. J. Lloret-Fillol**

1 – 17

Reaction Mechanisms of Single Metal Site Catalysts Supported on Covalent Organic Frameworks